AFM and Mössbauer spectrometry investigation of the nanocrystallization process in Fe–Mo–Cu–B rapidly quenched alloy

2007 J. Phys.: Condens. Matter 19 216219

(http://iopscience.iop.org/0953-8984/19/21/216219)

IOP PUBLISHING JOURNAL OF PHYSICS: CONDENSED MATTER

J. Phys.: Condens. Matter **19** (2007) 216219 (16pp) doi:10.1088/0953-8984/19/21/216219

AFM and Mössbauer spectrometry investigation of the nanocrystallization process in Fe–Mo–Cu–B rapidly quenched alloy

M Pavuk[1], M Miglierini[1,2], M Vujtek[2], M Mashlan[2], R Zboril[2] and Y Jiraskova[3]

[1] Department of Nuclear Physics and Technology, Slovak University of Technology, Ilkovičova 3, 812 19 Bratislava, Slovakia
[2] Nanomaterials Research Centre, Svobody 26, 771 46 Olomouc, Czech Republic
[3] Institute of Physics of Materials AS CR, Žižkova 22, 616 62 Brno, Czech Republic

Received 27 September 2006, in final form 10 April 2007
Published 1 May 2007
Online at stacks.iop.org/JPhysCM/19/216219

Abstract

In this paper, the effect of heat treatment on the development of nanocrystallites in rapidly quenched $Fe_{79}Mo_8Cu_1B_{12}$ alloy is investigated. The surface morphology is examined using non-contact mode atomic force microscopy (AFM). The results are compared with those obtained by transmission Mössbauer spectroscopy (TMS), conversion electron Mössbauer spectrometry (CEMS) and x-ray diffraction (XRD). It was found that the sample is not fully amorphous even in the as-quenched state. Minor amounts of bcc-Fe grains were detected on the wheel side of the ribbon-shaped samples while no indications of the crystalline phase were observed in the bulk. The crystallization onset is observed after annealing at 410 °C, when bcc-Fe nanograins are quite well developed. More intense crystallization is evidenced after annealing at higher temperatures, when the content of the crystalline phase increases progressively. The second crystallization, not discussed in the present paper, is characterized by the occurrence of additional crystalline phases, and appears after annealing at 650 °C. We suggest a crystallization model assuming no drastic change in the size of the primarily formed bcc-Fe nanograins with temperature as proved by XRD. The increase in annealing temperature induces the formation of a higher number of crystalline particles, which form large irregular agglomerates (80–130 nm in height), in accordance with the AFM data.

(Some figures in this article are in colour only in the electronic version)

1. Introduction

Nanocrystalline alloys exhibit unique structural and magnetic properties which are different from those of the conventional coarse-grained polycrystalline materials. The resulting microstructure is characterized by randomly oriented, ultrafine grains embedded in the residual

amorphous matrix, and the excellent soft magnetic response is related to averaging out the magnetocrystalline anisotropy via the magnetic interactions between these two constituent magnetic phases [1]. Such magnetic properties are very favourable for technical applications in power transformers, data communication components, pulsed transformers, choke coils, magnetic heads, sensors, and magnetic shielding [2].

Nanocrystalline materials can be produced using various methods and different starting phase (vapour, liquid, solid) which offer the formation of nanocrystalline structure either directly in one process (e.g. mechanical processing, vapour deposition) or indirectly through an amorphous precursor prepared by fast quenching of liquid alloy. In contrast to amorphous alloys produced with the same procedure and intensively investigated 20 years ago, the chemical composition of the amorphous precursor and the annealing conditions leading to the formation of nanocrystalline alloys differ [3–6]. While the amorphous alloys were mainly based on metal–metalloid systems, the amorphous precursors consist of some additional elements (Cu, Zr, Nb, Ta, etc) whose main role is to prevent the formation of large crystals and predominantly phases, e.g. borides, deteriorating the magnetic properties in the first stages of crystallization.

Copper addition, due to its very limited solubility in iron, forms small clusters, which can serve as sites for heterogeneous nucleation of Fe-based crystallites and contribute to an increase in their number by orders of magnitude in these alloys. In such a way it causes a decrease of the crystallization temperature and an increase of the nucleation rate. Copper-enriched clusters that formed prior to the onset of the crystallization process were detected, for example, in FINEMET-type alloys [7, 8] and in Zr-based NANOPERM-type alloys [9]. Boron enhances the thermal stability of the amorphous matrix and affects the homogeneity of the Fe precipitates [10].

From the point of view of excellent soft magnetic properties the main interest is to transform an amorphous precursor into pure α-Fe nanocrystals of small size. Therefore elements such as Nb or Zr are added. They do not easily form a solid solution with iron and they contribute to the limitation of the crystal growth because of their small diffusivity in an amorphous residual phase due to their large atomic size. They probably form an interface between the Fe-based nanocrystals and the amorphous matrix [11]. Very similar behaviour can be expected for Mo as well, due to its position in the periodic table.

Since temperature governs the structural arrangement and magnetic properties of the nanocrystalline alloys, both high-temperature-induced changes due to the annealing [12, 13] as well as low-temperature behaviour [14–17] were investigated. The main interest of the research groups is usually concentrated on the first crystallization step, when the nanocrystalline structure exhibits advantageous properties from both the structural and magnetic viewpoints [18]. Recently, an extensive study on the influence of temperatures exceeding the onset of the second crystallization step focused on revealing the relationship between microstructure and magnetic properties of ^{57}Fe phases, and their temperature dependences in NANOPERM-type ternary alloy was reported [19].

The present work was motivated by the need for a better understanding of Mo-containing nanocrystalline NANOPERM-type $Fe_{79}Mo_8Cu_1B_{12}$ alloy. The previous investigations of $Fe_{80-x}Mo_xB_{20}$ amorphous alloys confirmed that the addition of Mo enhances the crystallization temperature T_{cr} and decreases the Curie temperature T_C [20], while the amorphous alloys with changing Fe/B ratio and constant content of Mo have shown an increase in both T_{cr} and T_C with an increase in B content [21, 22]. Some investigations were also performed with Mo-containing FINEMET-type alloys. For such alloys, it was found that the addition of Mo enhances the stability of the amorphous alloy against crystallization, with a rate of the order of 15 K/at.% Mo [23].

The results published on Mo-containing NANOPERM-type alloys are not so widely spread up to now, even if the alloys show some interesting features [24]. Moreover, the system seems to be an appropriate candidate especially for case studies of hyperfine interactions using Mössbauer effect techniques [25]. An underlying goal of this research took into consideration the results of the previous reports which suggested that the formation of crystallites occurs more easily at the surface than in the bulk [26–29]. Differences in bulk and surface crystallization have already been pointed out in metal–metalloid glasses [30]. Surface crystallization and oxidation were shown to be responsible for the magnetoelastic effects observed in amorphous metals [31]. We also relay on the results concerning the mechanism of crystallization described earlier for Fe–B-type metallic glasses [32–34]. The attention of the present studies is therefore given to the structural changes that take place at the surface, in the subsurface layers, and in the bulk regions during the crystallization process.

To reach the specified aims we have employed a unique experimental approach which enables a complex description of the crystallization process by a combined use of several analytical techniques. The structural properties of the bulk of the samples are obtained by x-ray diffraction. This method provides information on the crystalline lattices present in the amorphous residual phase, including their qualitative (i.e., type of crystalline phase, lattice constant) as well as quantitative (relative fraction, grain size) characterization. The scanning depth is of the order of 10 μm, which is almost one half of the samples' volume as seen from one side of the investigated ribbon-shaped specimens. Mössbauer spectrometry is employed for the studies of structural and magnetic behaviour. Using ^{57}Fe atoms as probes, this method gives an unique opportunity for simultaneous inspection of the microstructural arrangement, including short-range order and magnetic behaviour via hyperfine interactions. Thus, unambiguous identification of Fe-containing crystalline but also disordered phases in the whole bulk of the investigated alloys is possible, and their relative contribution can be determined. By employing the detection of conversion electrons, the so-called conversion electron Mössbauer spectrometry (CEMS), we are able to derive information from the surface layers to a depth of about 200 nm. Consequently, differences between surface and bulk regions in the samples can be unveiled. It is noteworthy that Mössbauer spectrometry is suitable for the identification of Fe oxides, i.e. corrosion products. Scanning of the actual surface of the samples is performed by atomic force microscopy, which enables a description of the topological arrangement and size of the grains. The choice of the above-mentioned analytical tools ensures complementarity in combining the information obtained from the bulk and from the surface using different physical concepts.

2. Experimental details

As-quenched $Fe_{79}Mo_8Cu_1B_{12}$ alloy was prepared by planar flow casting in a form of 10 mm wide and 20–22 μm thick ribbon. Throughout this paper we will use the following convention as far as the ribbon surfaces are concerned. The side of the ribbon which was in a direct contact with the quenching wheel will be referred to as *the wheel side*. The opposite (top) side of the ribbon, i.e. the one which was exposed to the surrounding atmosphere, will be denoted as *the air side*. Both sides can be visually distinguished at first sight because the wheel side is dull or matt whereas the air side is shiny or gloss. The chemical composition of the alloy was checked by emission spectrometry with inductively coupled plasma.

Approximately 2 cm long specimens were annealed at temperatures ranging from 330 to 650 °C for 1 h in a vacuum. Individual treatment temperatures were chosen according to the differential scanning calorimetry (DSC) curve measured in Ar atmosphere using a Perkin-Elmer DSC 7 with a heating rate of 10 K min^{-1} [35]. ^{57}Fe Mössbauer spectra were obtained

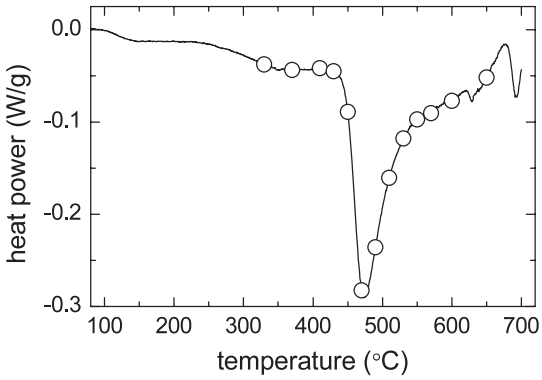

Figure 1. DSC curve (heating rate = 10 K min^{-1}) of as-quenched $Fe_{79}Mo_8Cu_1B_{12}$ ribbon with the indicated (O) temperatures of subsequent annealing treatment.

in scattering geometry by registering conversion electrons, the so-called conversion electron Mössbauer spectrometry (CEMS), and in transmission geometry by registering gamma-rays (transmission Mössbauer spectrometry—TMS) using a ^{57}Co(Rh) source in both modes. The CEMS detector was operated in an integral mode, i.e. covering a rather broad energy window of conversion electrons. Thus, the estimated screening depth is about 200 nm. The microstructure of as-quenched and nanocrystalline samples was analysed by x-ray diffraction (XRD) and atomic force microscopy (AFM). XRD patterns were obtained on an HZG-4 diffractometer in Bragg–Brentano geometry with Cu Kα radiation. The screening depth of x-rays is estimated to be less than 10 μm. For the acquisition of topographic images, an AFM Explorer microscope (ThermoMicroscopes, USA) was used. The microscope was placed on a pneumatic antivibration desk under a damping cover. The measurements were carried out in a non-contact mode under ambient conditions using silicon cantilevers of 1650-00 type from Veeco instruments with a tip radius of less than 10 nm.

3. Results and discussion

3.1. DSC and XRD analysis

The crystallization behaviour of the as-quenched $Fe_{79}Mo_8Cu_1B_{12}$ alloy was investigated using a DSC linear heating curve. The record in figure 1 is characterized by a massive exothermic dip, which corresponds to the main crystallization step. The onset temperature of the crystallization is expected at $T_{x1} \approx 445\,^{\circ}$C [35]. Taking into account the results of DSC measurements, we made decisions about the annealing temperatures.

XRD analysis of the as-quenched as well as annealed samples was performed at both the air and wheel sides of the ribbon. The XRD diffractograms obtained are presented in figure 2. Up to 430 °C, only broad reflections characteristic of amorphous structure are observed. Nevertheless, the presence of small maxima at the (110) and (220) angular positions of a bcc lattice are also revealed at 2θ values of 44.5° and 98.5°, respectively. This clearly indicates the presence of a crystalline phase dispersed within the amorphous matrix. Comparison of the principal x-ray reflections taken from both sides of the as-quenched $Fe_{79}Mo_8Cu_1B_{12}$ ribbon is illustrated in figure 3. Obviously, the crystallization at the air side is less developed.

It is noteworthy that the XRD patterns of the as-quenched ribbon do not exhibit any appreciable qualitative changes up to 430 °C, when additional diffraction peaks positioned at

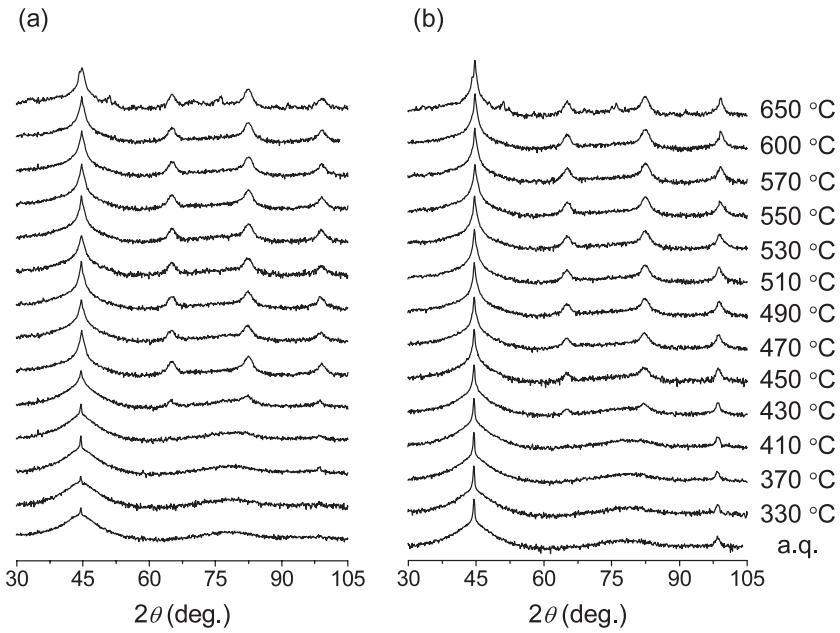

Figure 2. The XRD evolution of microstructure in $Fe_{79}Mo_8Cu_1B_{12}$ alloy with temperature of annealing (aq: as-quenched sample). The air (a) and wheel (b) sides of the ribbons were examined. The vertical axes are in logarithmic scale.

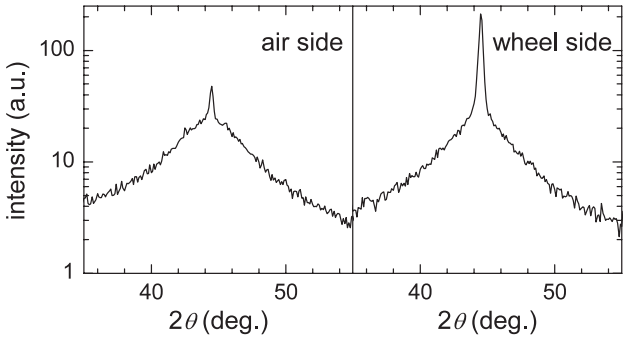

Figure 3. X-ray diffraction patterns of $Fe_{79}Mo_8Cu_1B_{12}$ sample taken from the air and wheel sides of the as-quenched ribbon.

2θ values of about 65° and 82° appear as further evidence of bcc (200) and (211) reflections. The first stage of transformation in $Fe_{79}Mo_8Cu_1B_{12}$ forms truly nanocrystalline bcc-Fe(Mo) grains. The supersaturation of bcc-Fe by Mo is evidenced by an increase of the lattice parameter against the value for pure bcc-Fe, as demonstrated in figure 4(a). Nevertheless, with rising temperature of annealing the lattice parameter approaches the value of pure bcc-Fe, which means that the amount of Mo in Fe decreases. (Additional confirmation of the effect of Mo incorporation into the bcc-Fe lattice is provided by the help of Mössbauer effect data in section 3.3.) Thus, the temperature of the onset of crystallization, T_{x1}, as derived from XRD data, can be determined to be 430 °C. This is by about 15 °C lower than that derived from

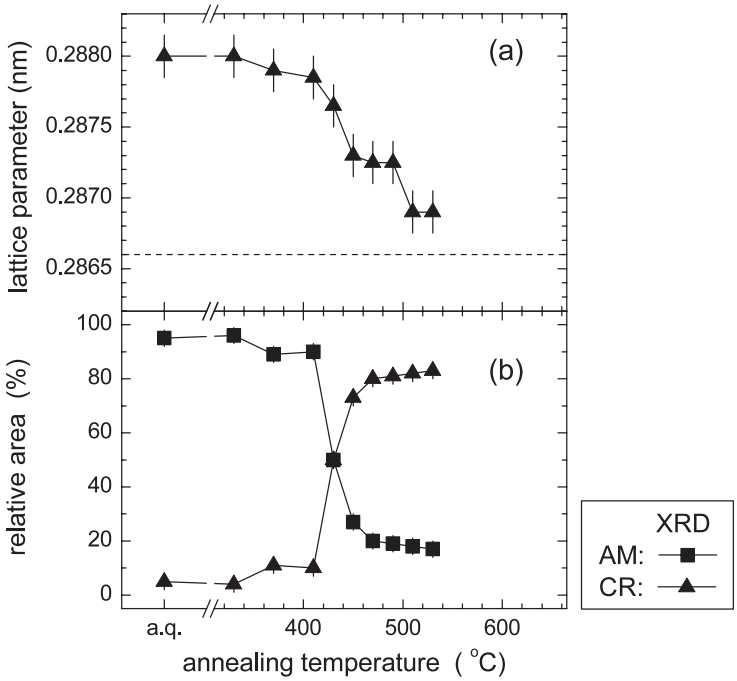

Figure 4. Lattice parameters of the bcc phase (a) and relative fraction of the crystalline (triangles) and amorphous (squares) phases (b) plotted against temperature of annealing as derived from XRD measurements. The connecting lines are only guides to the eye. The dashed line in (a) represents the lattice parameter of the pure bcc-Fe phase.

DSC [35], as expected due to the non-equivalent heating regime (isothermal versus dynamic treatment). The mean crystalline diameters calculated for the bcc-Fe phase from the Scherrer equation differ between 430 and 600 °C from ∼5–8 nm up to ∼10–12 nm. This fact indicates that the crystallization process results in the formation of bcc-Fe(Mo) nanograins of comparable size independently of the annealing temperature. However, their volume fraction in figure 4(b) increases progressively with the temperature as the intensities of the bcc reflections grow at the expense of the amorphous background.

It has been shown that the local atomic ordering in amorphous Fe–B-type alloys is of bcc type [36]. One of the best close-packed local arrangements of constituent atoms in Fe–B may be tetrahedral. A similar arrangement, slightly distorted and deformed, can be expected to be present after quenching. The glass-forming ability and/or stabilization of the amorphous phase depend among other parameters on the quenching rate, but also on the composition. A slight compositional gradient or solute drag across the ribbon thickness during solidification can be responsible for a different degree of crystallization on both surfaces of the ribbon. Possible differences in quenching rate on either surface could also be considered.

A bcc local ordering in amorphous Fe–Mo–Cu–B and subsequent immediate crystalline state can be relatively easily achieved by slight rearrangement over short distances with Mo being incorporated in the lattice in the form of supersaturated solid solution. At a higher temperature of annealing, a combination of B–Mo leads to phases with local ordering different from bcc—rhombohedral, tetragonal, hexagonal, etc. Thus, after annealing at 650 °C, traces of a mixture of tetragonal phase Mo_2FeB_2 ($P4/mbm$, no. 127) with parameters $a = 0.5775$ nm, $c = 0.3145$ nm and tetragonal Fe_3B ($I4$, no. 82), $a = 0.867\,36$ nm, $c = 0.431\,28$ nm are

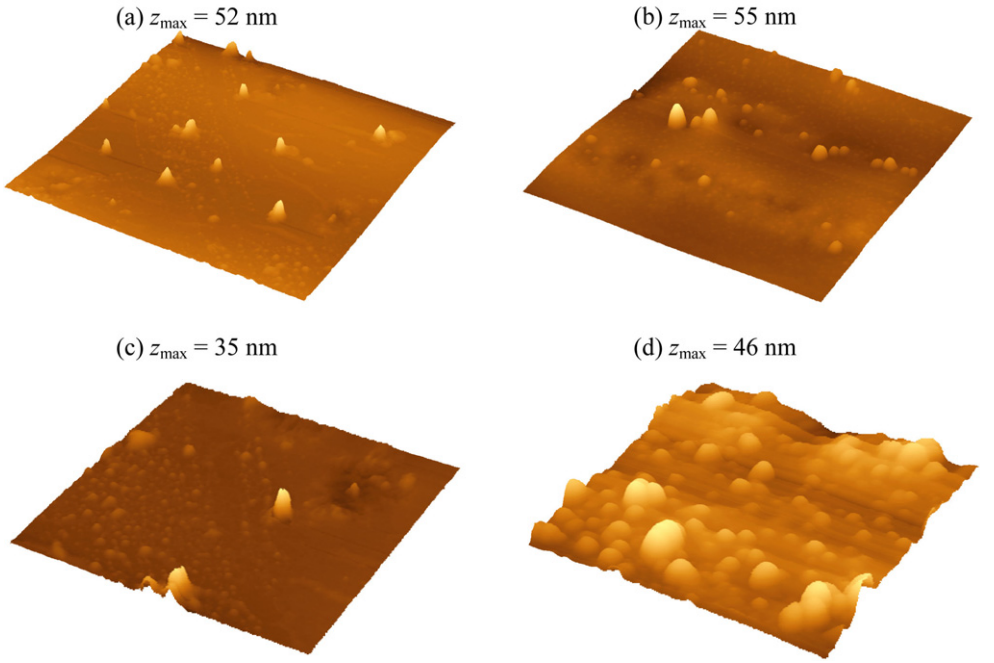

Figure 5. Three-dimensional AFM images of the air (a), (c) and wheel (b), (d) sides of $Fe_{79}Mo_8Cu_1B_{12}$ specimen. The scanned area was 2×2 μm^2 in images (a), (b) and 1×1 μm^2 in (c), (d). The maximum of the vertical scale is given by z_{max}.

observed. Since we focus on the progress of the first crystallization in this study, we have not performed more detailed analysis of the newly created crystalline phases.

3.2. AFM analysis

Surfaces of amorphous as well as nanocrystalline alloys can be effectively studied with the help of AFM [37–39], which is able to reveal surface features several nanometres in size. AFM images of the as-quenched ribbon are shown in figure 5.

The air side of the as-quenched $Fe_{79}Mo_8Cu_1B_{12}$ thin ribbon exhibits a smooth surface texture consisting of only a few extensions, as demonstrated by AFM scans in figures 5(a) and (c). On the other hand, the wheel side of the ribbon (figures 5(b) and (d)) demonstrates a wavy surface with notably more protrusions on it.

Two types of protrusions different in size are visible on the wheel surface in figure 5(b): a large number of single protrusions uniformly distributed with an average height of 1 nm and notably smaller number of larger humps, mostly 10–20 nm in height. The latter could confirm the evidence of crystallinity observed in the XRD patterns even at temperatures below 400 °C (figure 2). Positioning the scanning tip at different locations revealed even larger protrusions and no evidence of the smaller (1 nm) ones. The waves, visible on the wheel side of the ribbon, most probably reflect the natural surface imperfections of the quenching copper wheel which is used for the production of rapidly quenched precursors. That is why we have concentrated on the inspection of the air (visually shiny) side of the ribbons.

Examples of AFM scans taken from the air side of thermally treated samples are illustrated in figure 6. From this figure, it is clearly seen that the density of the larger bright spots is directly related to the temperature of annealing, i.e. to the relative fraction of nanocrystallites formed in

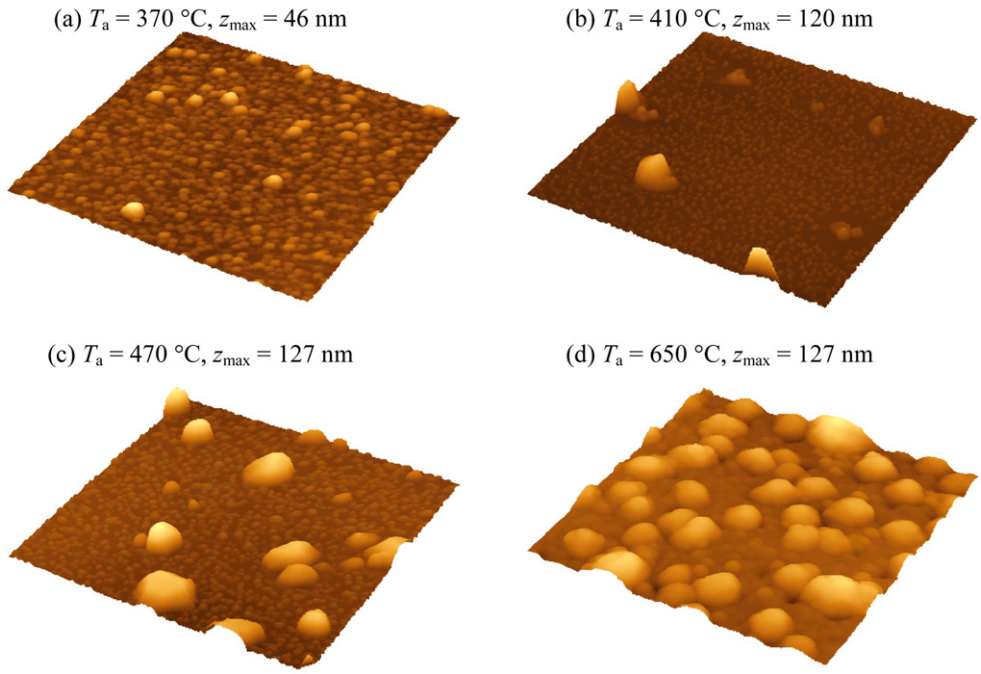

Figure 6. Three-dimensional AFM surface images of the $Fe_{79}Mo_8Cu_1B_{12}$ specimen after annealing for 1 h at T_a = 370, 410, 470 and 650 °C. The scanned area was 2 × 2 μm^2 and all scans were performed on the air side of the ribbons.

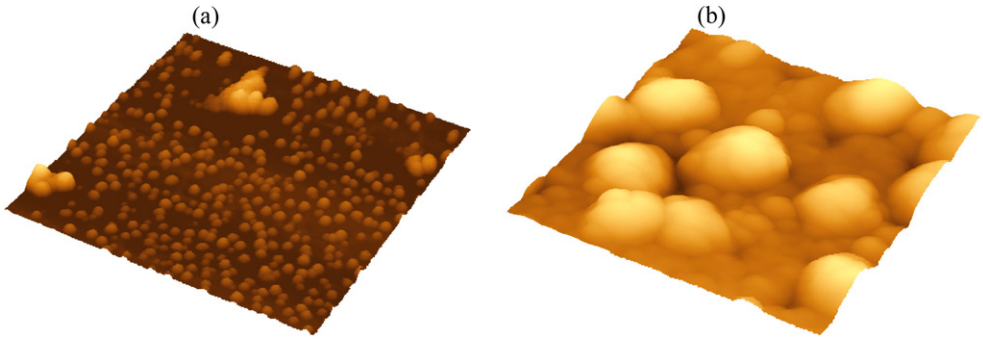

Figure 7. Three-dimensional AFM surface images of the $Fe_{79}Mo_8Cu_1B_{12}$ specimen after annealing for 1 h at T_a = 410 °C (a) and 650 °C (b). The scanned area was 1 × 1 μm^2 and the scans were performed on the air side of the ribbons.

the alloy. The surface morphology observed at 410 °C is especially interesting. It shows very few large objects (z_{max} = 120 nm) of non-uniform shape that are surrounded by small-sized protrusions with rather uniform height of about 10 nm and closely packed structure. The latter could be ascribed to individual crystalline grains. The irregular shape and the high values of vertical dimensions, which are far from the crystallite diameters obtained from XRD, suggest that the large bright objects correspond to agglomerates of nanograins.

This hypothesis is supported with the help of figure 7(a) where a three-dimensional (3D) scan of a 1 × 1 μm^2 area of the 410 °C annealed sample is illustrated. One can clearly see

flat regions which surround three big agglomerates. These featureless surfaces indicate that the agglomerates have consumed (via diffusion) those Fe atoms that established a bcc crystalline phase. The number of these agglomerates increases with temperature, and this finding is in accordance with the Mössbauer spectrometry data (see section 3.3). In the sample annealed at 650 °C, the clusters of crystalline grains cover the major part of the scanned surface as demonstrated in figure 7(b). Their enormous dimensions can be ascribed not only to an enhanced growth of the bcc-Fe grains but also to the formation of other crystalline phases (Mo_2FeB_2, Fe_3B) during this second crystallization step as evidenced by XRD and DSC.

To conclude this section we would like to make a comment on the nature of apparent differences in the size of crystals derived from XRD and AFM data. In XRD, the size of grains is estimated using the generally accepted procedure based on the Scherrer equation, silently accepting the conditions (related to, for example, the shape of the grains) under which it was derived. Taking into consideration the real shape of the grains, their size might be slightly underestimated.

In AFM, one has to consider such effects as the profile of the scanning tip, surface oxidation, and/or surface humidity of the sample, which might affect the size of the examined features.

The radius of the scanning tip (10 nm in our case) contributes to an increase in the observed lateral dimensions especially when several small objects are located close to each other, i.e. the objects are smaller and closer together than the tip curvature. Mutual proximity of several protrusions could affect the vertical dimensions, too, notably because of the non-contact mode of the registration used. In addition, vertical dimensions can be affected by oxidation and/or humidity. We can exclude the influence of oxidation because no traces of oxides were revealed either by XRD or by CEMS (see section 3.3). If there were any oxidation it is reasonable to assume that it would affect the whole surface, and that is why it should be detectable. In order to assess the influence of humidity which might be possibly adsorbed especially at the protrusions, we cleaned some samples immediately before scanning. No appreciable differences in the images acquired from the cleaned and as-received samples were revealed. On the other hand, the quality (cleanness) of the scanning tip was found to be decisive for obtaining good scans. In order to record images suitable for further processing, the tip had to be exchanged for a new one after scanning several samples.

Based on the above discussion and considering the size of the grains (∼10 nm) determined from XRD, we propose that agglomeration of crystallites is a possible explanation for the observed big features in our AFM scans. Because of their size, independent grains, emerging from the ribbon surface, would have rather high surface energy. Thus, agglomeration is an effective way of decreasing the surface energy, notably at the higher temperatures of annealing. The relative abundance of protrusions correlates with the amount of crystallites (temperature of annealing) whereas the nature of the formed crystalline phases is determined by XRD and Mössbauer spectrometry.

3.3. CEMS and TMS analysis

According to the XRD and AFM results (see figures 3 and 5), the crystalline species were found even in the as-quenched alloy with a higher content of the bcc-Fe(Mo) phase on the wheel side of the ribbon. As demonstrated in figure 8, CEMS analysis detected an occurrence of bcc-Fe(Mo) on this side of the ribbon only. The corresponding Mössbauer component is indicated in the wheel-side spectrum (middle part of figure 8) by a grey shaded six-line pattern. Four lines of this sextet (hyperfine field $B_{hf} = 32.60 \pm 0.1$ T, isomer shift $\delta = 0.00 \pm 0.02$ mm s^{-1}), which are marked with arrows, are clearly visible as satellite lines to the central signal, whereas

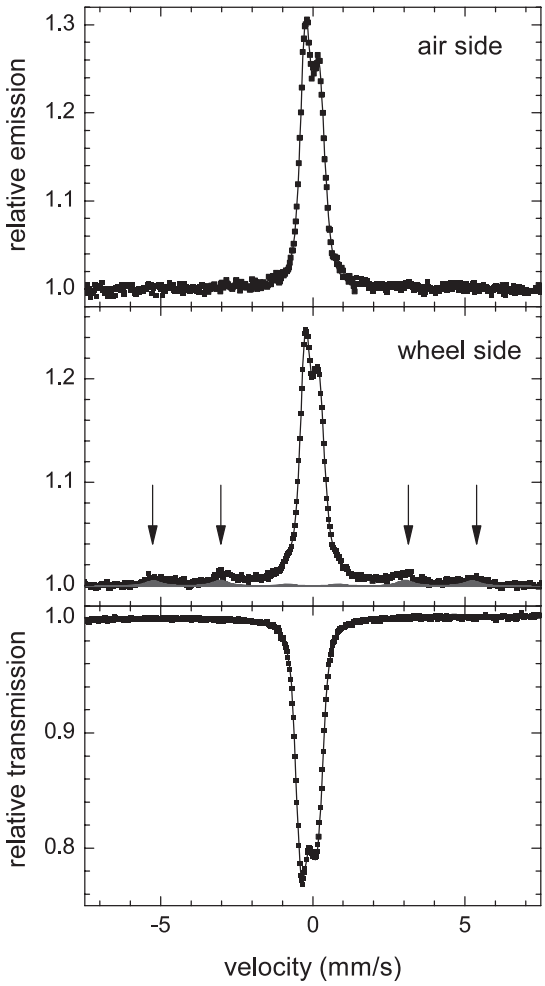

Figure 8. Mössbauer spectra of the as-quenched $Fe_{79}Mo_8Cu_1B_{12}$ alloy: CEMS spectra taken from the air and wheel sides of the ribbon-shaped sample, and TMS spectrum (bottom picture). The arrows indicate the positions of the outer four lines of the crystalline sextet (grey filled line).

its two inner lines overlap with the central amorphous doublet. No traces of any Fe-containing crystalline phase were identified by TMS and/or by CEMS on the air side of the ribbon within the detection limits of both techniques. It is noteworthy that for the sake of clearer presentation of the spectral details we show all Mössbauer spectra in a velocity range restricted by the highest hyperfine splitting observed. Nevertheless, to check for the eventual occurrence of magnetic oxides we have recorded the spectra also in a broad velocity range (± 12 mm s^{-1}). No traces of Fe-containing oxides were revealed and neither were other oxides by XRD (within the detection limits of both methods). The Mössbauer signal, stemming from non-magnetic iron oxides, might possibly be hindered by the broad amorphous central line, but because of the XRD results this alternative is not very likely.

Taking into consideration the results from XRD, AFM, and CEMS, we can conclude that the size (and/or the number) of the crystallites on the air side of the as-quenched ribbon is fairly low. Moreover, they are only few, so no Mössbauer signal could be detected because of

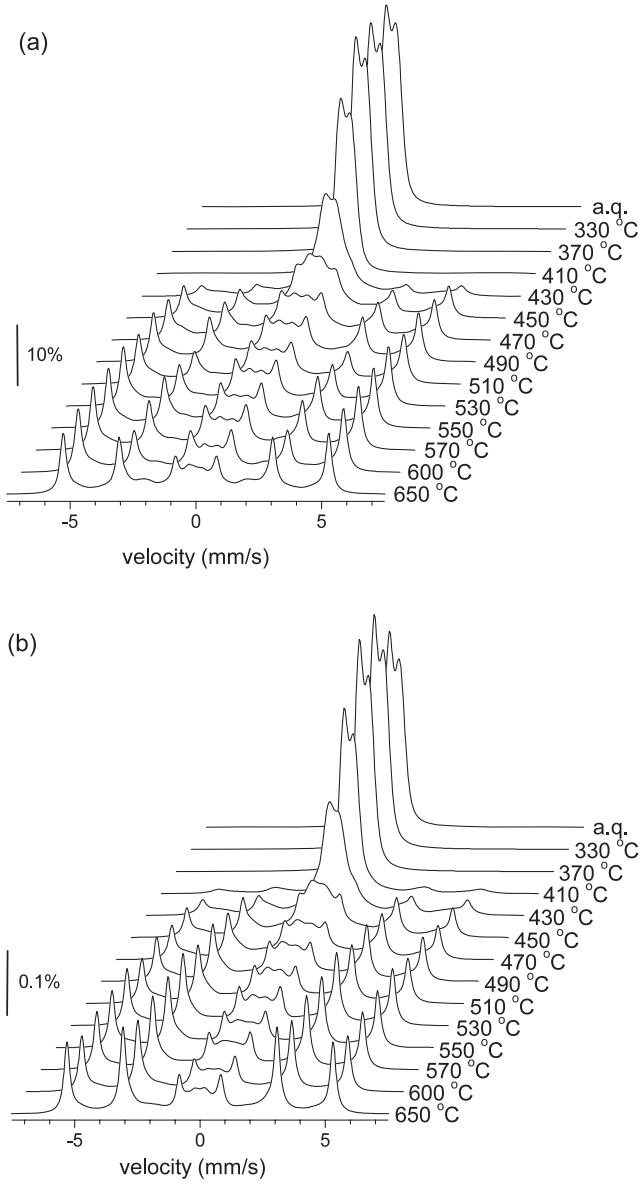

Figure 9. Transmission (a) and conversion electrons (b) Mössbauer spectra for the $Fe_{79}Mo_8Cu_1B_{12}$ specimen in the as-quenched (aq) and annealed states. The transmission spectra are vertically flipped for the sake of better presentation.

superparamagnetic behaviour and/or thermal relaxation of magnetic moments. Consequently, CEMS experiments were performed on the air side of the ribbon.

Figure 9 shows transmission and CEMS Mössbauer spectra of the as-quenched and thermally treated samples. The samples annealed at low enough temperatures (below the onset of the crystallization) exhibit broadened doublets. They indicate a presence of the non-magnetic atomic regions with a disordered structural arrangement which were reconstructed with the help of distributions of quadrupole splitting. After the onset of crystallization,

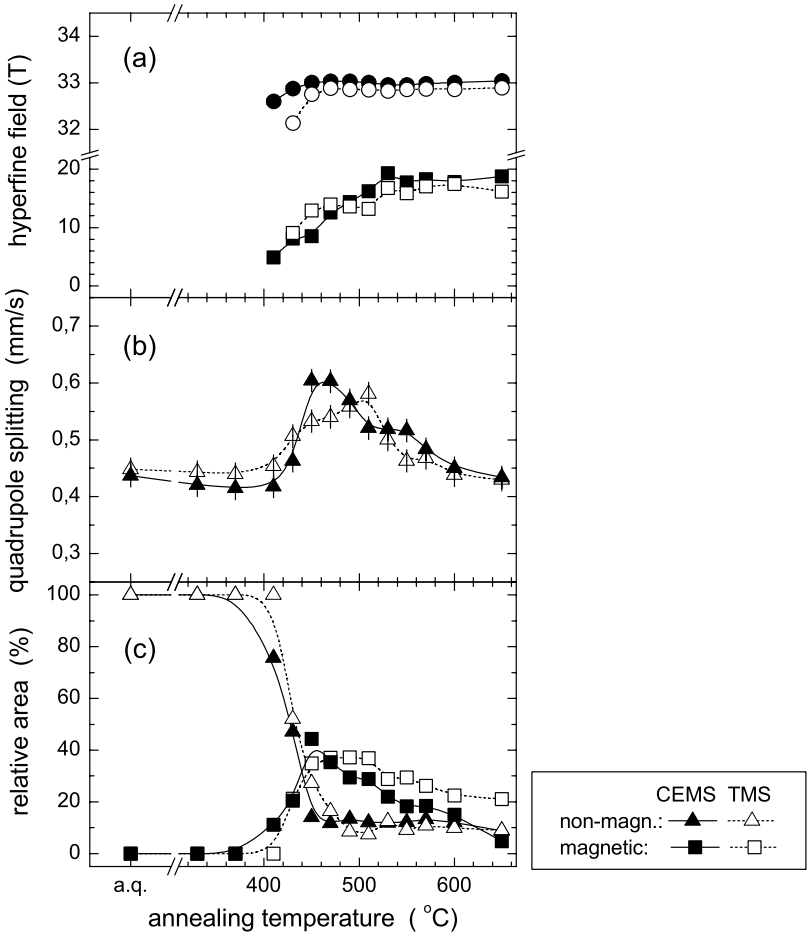

Figure 10. Hyperfine fields of crystalline phase (circles) and magnetic part of the residual amorphous matrix (a), average quadrupole splitting of the non-magnetic amorphous regions (b), and relative fraction of magnetic (squares) and non-magnetic (triangles) amorphous regions (c) plotted against temperature of annealing as derived from CEMS (solid symbols) and TMS measurements (open symbols).

narrow lines representing bcc-Fe crystallites appear in the outer regions of the Mössbauer spectra. At the same time, the central part of the Mössbauer spectra decreases in intensity and further broadening is observed. This indicates that weak magnetic interactions show up in the amorphous residual matrix as a consequence of the following two effects: (i) compositional modification of the amorphous rest due to a segregation of Fe atoms into bcc-Fe crystalline phase, which in turn enhances the effective concentration of the other constituent elements and induces a rearrangement of chemical and/or topological short-range order, and (ii) as the relative fraction of the crystalline phase increases, the individual bcc-Fe grains start to cooperate among themselves and the resulting magnetic exchange interactions polarize the originally non-magnetic amorphous matrix.

The above interpretation is supported by figure 10, where the average values of the hyperfine field and quadrupole splitting distributions as well as relative fractions of these components, representing the amorphous residual matrix and hyperfine fields of the crystalline

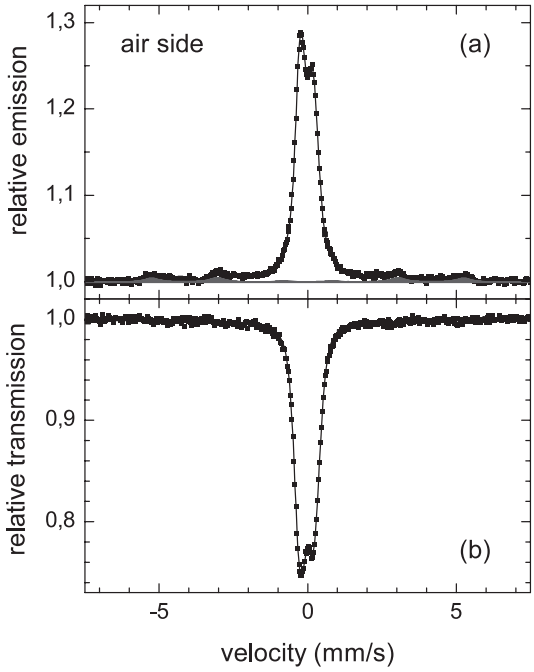

Figure 11. CEMS (a) and TMS (b) spectrum of the $Fe_{79}Mo_8Cu_1B_{12}$ alloy annealed at 410 °C/1 h.

phase, are plotted against the temperature of annealing. The onset of the crystallization is characterized by a significant increase of the quadrupole splitting, even though its relative fraction decreases. At the same time, the contribution of the magnetic regions in the amorphous remainder of the sample increases. Both effects indicate the formation of the nearest neighbourhoods of Fe resonant atoms with elevated magnetic dipole and electric quadrupole interactions due to the enhanced concentration of boron and molybdenum, respectively. This is due to the segregation of Fe into the crystallites, thus changing the original composition as well as the chemical and topological short-range order of the amorphous remainder of the sample.

The increase in the quadrupole splitting values (and also the contribution of magnetic amorphous regions) culminates at 470 and 510 °C for the surface (CEMS) and bulk (TMS) of the ribbons, which coincides with the maximum and the end of the first crystallization peak, respectively (see figure 1). For higher temperatures of annealing a decrease of the mentioned parameters is observed because the overall fraction of the amorphous residual phase reduces at the expense of the crystallites. The latter grow in size and amount, thus reinforcing the magnetic exchange interactions among them, which in turn also polarizes the amorphous rest and gives rise to the value of its average hyperfine field (figure 10(a)).

The first indication of a spectral signal from bcc-Fe comes from the surface of the sample annealed at 410 °C; a detailed comparison of the corresponding CEMS (air side) and TMS spectra is given in figure 11. While the spectrum obtained by TMS does not show any traces of the crystallization, the CEMS technique, which is sensitive to close-to-surface layers of about 200 nm thickness, has revealed traces of a sextet already emerging at this temperature. This occurrence can be explained either by a thermal gradient produced during a thermal treatment as suggested in [40] or as a consequence of the structural inhomogeneities in the original as-quenched precursor as already discussed in section 3.1.

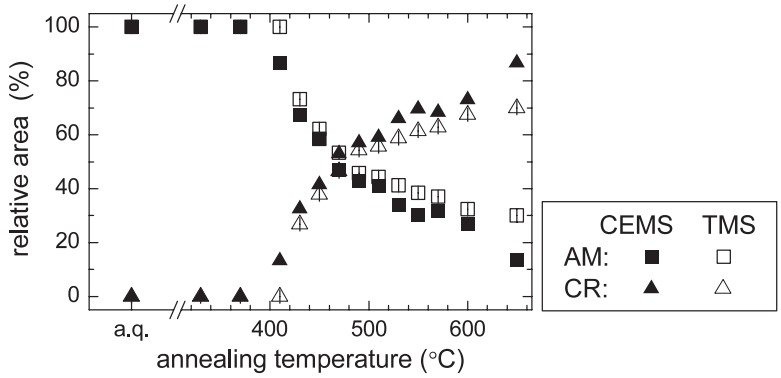

Figure 12. Relative fraction of the crystalline (triangles) and amorphous (squares) phases plotted against temperature of annealing as derived from CEMS (solid symbols) and TMS measurements (open symbols).

According to the spectral parameters ($B_{\mathrm{hf}} = (32.89 - 33.01) \pm 0.1$ T, $\delta \sim 0.00 \pm 0.02$ mm s^{-1}), the crystallites formed in the near-surface region belong to bcc-Fe phase. Lower B_{hf} than that of a bulk bcc-Fe (33.1 T) is caused by a combination of two effects: (i) magnetic relaxation phenomena which are pronounced in the early stages of the crystallization when the size of the grains is small (∼5 nm) and their relative fraction is also low (∼10%), and (ii) small inclusions of Mo into the bcc lattice as evidenced from XRD by an increase of the lattice parameter (see figure 4(a)). Both effects weaken with progressing crystallization (temperature of annealing) as also demonstrated in figure 10(a) when the hyperfine fields reach the values close to that for pure bcc-Fe. Distinctions between surface and bulk crystallization are demonstrated by very small deviations in the hyperfine fields towards the high temperature of annealing (figure 10(a)). They are quite pronounced in the early stages of the crystallization (low temperature of annealing), which is an indication of a different crystallization kinetics.

The evolution of the relative spectral areas of the crystalline and amorphous regions in the $Fe_{79}Mo_8Cu_1B_{12}$ alloy is plotted as a function of annealing temperature in figure 12. The error range in the determination of the relative fraction is comparable with the size of the symbols used. The results, presented in this figure, are in good agreement with the previous observations of the crystallization processes in the amorphous and nanocrystalline alloys [26–29] that the crystallization process starts on the surface at lower annealing temperature in comparison with the bulk. The temperature of the onset of (surface) crystallization was determined to be 410 °C.

4. Conclusions

We have investigated the progress of the crystallization in the $Fe_{79}Mo_8Cu_1B_{12}$ alloy as a function of temperature of annealing. The $Fe_{79}Mo_8Cu_1B_{12}$ NANOPERM-type alloy studied is not fully amorphous even in the as-quenched state. The presence of a small amount of crystalline bcc-Fe phase was confirmed at the surface by AFM and XRD, and in the close surface layers by CEMS on the wheel side of the ribbon. No indications of crystallites were found in the bulk of the as-quenched alloy by TMS and/or on the air surface by CEMS, which was therefore chosen for investigations of the onset of surface crystallization in the present paper. The crystallization process is accompanied by a formation of the bcc-Fe grains with the size of about 15 nm as determined from XRD; however, the relative fraction of the crystalline phase increases more significantly, mainly between 410 and 530 °C, as proved by

CEMS and TMS. AFM observations reveal that the crystalline grains form large agglomerates (∼80–130 nm in height) of irregular shape, the number of which increases with temperature.

The temperature of the onset of the bulk crystallization was determined from DSC to be 445 °C [35]. XRD shows the appearance of thermally induced crystallization at 430 °C. This apparent deviation can be explained by different temperature regimes applied during the DSC scan (dynamic treatment) and sample annealing (isothermal treatment). On the other hand, CEMS experiments have confirmed that bcc-Fe nanocrystals are already formed after heat treatment at 410 °C. This implies that crystallization starts earlier on the surface of the ribbon than in its bulk as frequently observed in amorphous alloys. This might be caused by an insufficient quenching rate or glass-forming ability of the surface regions which, in turn, triggers the formation of the nucleation centres. The minimum crystallization temperature observed by CEMS corresponds well with the first indications of the crystalline agglomerates in AFM.

Finally, we would like to make a comment on the nanocrystals at the air side of the ribbon in the as-quenched state, which were observed by AFM (section 3.2), with difficulty identified in XRD (section 3.1) and not detected by CEMS (section 3.3). Apart from the explanation proposed in section 3.3, we can speculate that XRD detects the crystals also at the air side even if they are in fact formed at the wheel side of the ribbon. This might be possible if we assume that the penetration depth of x-rays is about 11–12 μm and, at the same time, the thickness of the sample is inhomogeneous as a result of the preparation conditions. To confirm this hypothesis, further experiments are now in progress. Thus, very tiny nanocrystals created at the air surface are only identified by AFM, and they are under the detection limits of both XRD and CEMS.

Acknowledgments

The authors wish to acknowledge E Illeková and P Švec (Bratislava) for assistance with DSC and XRD measurements, respectively, and D Janičkovič (Bratislava) for sample preparation. This work was supported by the grants VEGA 1/4011/07, FR/SL/FEISTU/04, Czech Science Foundation 202/05/2111, MSM6198959218 and 1M6198959201.

References

[1] Gómez-Polo C, Pérez-Landazabal J I, Recarte V, Campo J, Marín P, López M, Hernando A and Vázquez M 2002 *Phys. Rev.* B **66** 012401
[2] McHenry M E and Laughlin D E 2000 *Acta Mater.* **48** 223
[3] Yoshizawa Y, Oguma S and Yamauchi K 1988 *J. Appl. Phys.* **64** 6044
[4] Suzuki K, Kataoka N, Inoue A, Makino A and Masumoto T 1990 *Mater. Trans. JIM* **31** 743
[5] Willard M A, Laughlin D E, McHenry M E, Thoma D, Sickafus K, Corss J O and Harris V G 1998 *J. Appl. Phys.* **84** 6773
[6] Herzer G 1993 *Phys. Scr.* T **49** 307
[7] Hono K, Li J-L, Ueki Y, Inoue A and Sakurai T 1993 *Appl. Surf. Sci.* **67** 398
[8] Ayers J D, Harris V G, Sprague J A, Elam W T and Jones H N 1998 *Acta Mater.* **46** 1861
[9] Zhang Y, Hono K, Inoue A and Sakurai T 1996 *Scr. Mater.* **34** 1705
[10] Swilem Y, Sobczak E, Nietubyć R and Ślawska-Waniewska A 2005 *Physica* B **364** 71
[11] Swilem Y, Sobczak E, Nietubyć R, Dluzewski P and Ślawska-Waniewska A 1999 *J. Alloys Compounds* **286** 103
[12] Kopcewicz M, Grabias A and Williamson D L 1997 *J. Appl. Phys.* **82** 1747
[13] Yoon S H, Kim S B, Lee H M and Kim Ch S 2003 *J. Magn. Magn. Mater.* **254/255** 507
[14] Ślawska-Waniewska A and Grenèche J M 1997 *Phys. Rev.* B **56** R8491
[15] Suzuki K and Cadogan J M 1998 *Phys. Rev.* B **58** 2730
[16] Balogh J, Bujdosó L, Kaptás D, Kemény T, Vincze I, Szabó S and Beke D L 2000 *Phys. Rev.* B **61** 4109

[17] Kemény T, Kaptás D, Kiss L F, Balogh J, Vincze I, Szabó S and Beke D L 2000 *Hyperfine Interact.* **130** 181
[18] Hono K 2002 *Prog. Mater. Sci.* **47** 621
[19] Stankov S, Sepiol B, Kaňuch T, Scherjau D, Würschum R and Miglierini M 2005 *J. Phys.: Condens. Matter* **17** 3183
[20] Nielsen H J V 1979 *Solid State Commun.* **30** 239
[21] Nielsen H J V 1980 *J. Magn. Magn. Mater.* **19** 138
[22] Majumdar A K 1979 *Solid State Commun.* **29** 85
[23] Franco V, Conde C F, Conde A and Ochin P 2001 *J. Non-Cryst. Solids* **287** 366
[24] Idzikowski B, Baszynski J, Skorvanek I, Müller K-H and Eckert D 1998 *J. Magn. Magn. Mater.* **177–181** 941
[25] Miglierini M, Degmová J, Kaňuch T, Švec P, Illeková E and Janičkovič D 2005 *Properties and Applications of Nanocrystalline Alloys from Amorphous Precursors* ed B Idzikowski *et al* (Dordrecht: Kluwer) pp 421–36
[26] Grabias A, Kopcewicz M and Idzikowski B 1999 *Nanostruct. Mater.* **12** 899
[27] Grabias A, Kopcewicz M and Idzikowski B 1999 *Mater. Res. Soc. Symp. Proc.* **577** 543
[28] Miglierini M and Seberíni M 2002 *Phys. Status Solidi* a **189** 351
[29] Miglierini M, Seberíni M, Tóth I and Vitázek K 2003 *J. Magn. Magn. Mater.* **265** 243
[30] Köster U 1988 *Mater. Sci. Eng.* **97** 233
[31] Gonser U, Ackermann M and Wagner H-G 1983 *J. Magn. Magn. Mater.* **31–34** 1605
[32] Köster U and Herold U 1978 *Scr. Metall.* **12** 75
[33] Ruckman M W, Levy R A, Kessler A and Hasegawa R 1980 *J. Non-Cryst. Solids* **40** 393
[34] Herold U, Köster U and Dirks A G 1980 *J. Magn. Magn. Mater.* **19** 152
[35] Illeková E, Janičkovič D, Miglierini M, Škorvánek I and Švec P 2006 *J. Magn. Magn. Mater.* **304** e636
[36] Hirotsu Y, Ohkubo T and Matsushita M 1998 *Microsc. Res. Tech.* **40** 284
[37] Le A-T, Kim Ch-O, Chau N, Cuong N D, Tho N D, Hoa N Q and Lee H 2006 *J. Magn. Magn. Mater.* **307** 178
[38] Miglierini M, Kaňuch T, Švec P, Krenický T, Vůjtek M and Zbořil R 2006 *Phys. Status Solidi* b **243** 57
[39] Miglierini M, Kaňuch T, Jirásková Y, Mashlan M, Zbořil R and Vůjtek M 2006 *Hyperfine Interact.* **165** 75
[40] Bibicu I, Garitaonandia J S, Plazaola F and Apiñaniz E 2001 *J. Non-Cryst. Solids* **287** 277